Key Points:
- Postmidnight field-aligned irregularities occur within plasma bubbles and coincide with kilometer-scale plasma density irregularities
- Equatorward thermospheric winds at low latitudes could affect generation of postmidnight field-aligned irregularities
- Equatorward thermospheric winds associated with midnight temperature maximum could increase the growth rate of Rayleigh-Taylor instability

Coordinated observations of postmidnight irregularities and thermospheric neutral winds and temperatures at low latitudes

Tam Dao[1,2] (ID), Yuichi Otsuka[1] (ID), Kazuo Shiokawa[1] (ID), Michi Nishioka[3] (ID), Mamoru Yamamoto[4] (ID), Suhaila M. Buhari[5] (ID), Mardina Abdullah[6] (ID), and Asnawi Husin[7]

[1]Institute for Space-Earth Environmental Research, Nagoya University, Nagoya, Japan, [2]Ho Chi Minh City Institute of Physics, VAST, Ho Chi Minh City, Vietnam, [3]National Institute of Information and Communications Technology, Koganei, Japan, [4]Research Institute for Sustainable Humanosphere, Kyoto University, Kyoto, Japan, [5]Department of Physics, Universiti Teknologi Malaysia, Johor Bahru, Malaysia, [6]Space Science Centre, Universiti Kebangsaan Malaysia, Bangi, Malaysia, [7]National Institute of Aeronautics and Space (LAPAN), Jakarta, Indonesia

Abstract We investigated a postmidnight field-aligned irregularity (FAI) event observed with the Equatorial Atmosphere Radar at Kototabang (0.2°S, 100.3°E, dip latitude 10.4°S) in Indonesia on the night of 9 July 2010 using a comprehensive data set of both neutral and plasma parameters. We examined the rate of total electron content change index (ROTI) obtained from GPS receivers in Southeast Asia, airglow images detected by an all-sky imager, and thermospheric neutral winds and temperatures obtained by a Fabry-Perot interferometer at Kototabang. Altitudes of the F layer ($h'F$) observed by ionosondes at Kototabang, Chiang Mai, and Chumphon were also surveyed. We found that the postmidnight FAIs occurred within plasma bubbles and coincided with kilometer-scale plasma density irregularities. We also observed an enhancement of the magnetically equatorward thermospheric neutral wind at the same time as the increase of $h'F$ at low-latitude stations, but $h'F$ at a station near the magnetic equator remained invariant. Simultaneously, a magnetically equatorward gradient of thermospheric temperature was identified at Kototabang. The convergence of equatorward neutral winds from the Northern and Southern Hemispheres could be associated with a midnight temperature maximum occurring around the magnetic equator. Equatorward neutral winds can uplift the F layer at low latitudes and increase the growth rate of Rayleigh-Taylor instabilities, causing more rapid extension of plasma bubbles. The equatorward winds in both hemispheres also intensify the eastward Pedersen current, so a large polarization electric field generated in the plasma bubble might play an important role in the generation of postmidnight FAIs.

1. Introduction

Plasma bubbles are localized plasma density depletions in the ionosphere at equatorial and low-latitude regions. They contain plasma density irregularities with various sizes [e.g., *Woodman and Lahoz*, 1976; *Basu et al.*, 1978; *Otsuka et al.*, 2004]. Using VHF, UHF, and L band radars at magnetically low latitudes, intense coherent echoes caused by the Bragg scattering from field-aligned irregularities (FAIs) with the size of half the radar wavelength have been observed as manifestations of plasma bubbles [e.g., *Woodman and LaHoz*, 1976]. *Tsunoda et al.*, 1982 showed that FAIs observed using the ALTAIR radar were collocated with plasma depletions measured using the Atmosphere Explorer-E satellite. Plasma irregularities in the ionosphere can cause scintillation of radio waves passing through the ionosphere and can degrade ground–satellite communication and satellite-based positioning systems, such as the Global Positioning System (GPS). Therefore, ionospheric plasma bubbles or irregularities are important in ionospheric research. It is well known that plasma bubbles are generated via Rayleigh–Taylor (RT) instabilities that occur after sunset when the eastward electric fields increase. Enhancement of the eastward electric field occurring around the evening terminator in the equatorial ionosphere, known as prereversal enhancement (PRE), increases the extent of upward $E \times B$ drift. The rate at which plasma bubbles occur depends on the local time, the season, and solar activity. In the Asian longitudinal sector, plasma bubbles occur frequently after sunset in equinoxes during high solar activity [*Tsunoda*, 1985; *Burke et al.*, 2004; *Nishioka et al.*, 2008]. Such local-time, seasonal, and solar-activity dependences could be attributed to the magnitude of the eastward electric field at the magnetic equator, which is one of the most important parameters in relation to plasma bubble generation.

During the most recent solar minimum period, FAIs were commonly observed after midnight using VHF radars at low magnetic latitudes in India, Indonesia, and the southern part of China [*Otsuka et al.*, 2009, 2012; *Patra et al.*, 2009; *Li et al.*, 2011; *Ajith et al.*, 2015]. The C/NOFS satellite has been used to observe post-midnight plasma density irregularities [*Dao et al.*, 2011]. Recent studies show some typical characteristics of postmidnight FAIs differed from those of postsunset FAIs. Postmidnight FAIs occur frequently around the June solstice and tend to propagate westward [*Otsuka et al.*, 2009, 2012], while postsunset FAIs appear commonly in equinoxes and propagate eastward. Most postmidnight FAIs do not reach an altitude of 450 km, while postsunset FAIs develop quicker to higher altitudes (above 500 km) [*Dao et al.*, 2016].

By carrying out multibeam observations of FAIs using the Equatorial Atmosphere Radar (EAR) in Indonesia, *Ajith et al.* [2015] classified postmidnight FAIs into two categories: the evolutionary type which is generated within the EAR's field of view (FOV); and drifting-in type, which is formed elsewhere and then drifts into the radar's FOV. Some of the drifting-in FAIs may correspond to the FAIs associated with medium-scale traveling ionospheric disturbances, which appear frequently at midlatitudes and tend to propagate to lower latitudes [*Saito et al.*, 2008; *Otsuka et al.*, 2009; *Candido et al.*, 2011]. The other possibility for drifting-in FAIs is that they exist within plasma bubbles generated elsewhere and move into the EAR's FOV just after midnight. The evolving type of FAIs could exist in plasma bubbles that are growing. *Dao et al.* [2016] used the EAR to examine the growth of freshly evolving postmidnight FAIs and suggested that the plasma bubbles associated with fresh postmidnight FAIs are initiated around midnight. Just after sunset, the enhanced eastward electric field is the main cause of plasma bubbles via RT instabilities. However, the electric field during the night is westward [*Fejer et al.*, 1991], which makes the RT growth rate negative. *Nishioka et al.* [2012] have suggested that uplift of the *F* layer may play an important role in enhancing the RT growth rate by increasing the gravity-driven eastward electric current during conditions of low solar activity. Using a longitudinal chain of ionosondes, *Ajith et al.* [2015] measured frequent uplifts of the *F* layer around midnight during the low solar activity at the June solstice. *Nicolls et al.* [2006] showed that uplifts of the *F* layer around midnight could be related to a decreasing westward electric field, which in turn may be caused by a change in the wind system related to the midnight pressure bulge associated with the midnight temperature maximum (MTM).

Maruyama et al. [2008] reported that the MTM during summer is associated with a convergence of equatorward thermospheric winds near local midnight. This causes a density maximum, and the MTM then appears via adiabatic heating [*Herrero et al.*, 1993]. *Meriwether et al.* [2008] showed that the nighttime meridional wind toward the equator results from thermospheric tidal activity that contributes to the formation of the MTM. *Huba and Krall* [2013] calculated the growth rate of RT instabilities using the SAMI3/ESF model. They showed that equatorward winds at low latitudes (i.e., at nonzero inclination of the magnetic field) could destabilize the bottomside of the *F* layer by decreasing the Pedersen conductivity. However, there have been no reported observations of thermospheric neutral winds or temperatures during postmidnight irregularities.

The present paper reports a case of postmidnight FAIs that were observed with the EAR in Indonesia on 9 July 2010. This was a case of postmidnight FAIs recorded during 2010–2013 in which thermospheric neutral winds and temperatures were detected. The FAIs are compared with 630 nm airglow images, kilometer-scale plasma irregularities, ionospheric *F* layer altitudes, and thermospheric neutral winds and temperatures observed with multiple instruments at Kototabang, Indonesia, and in Southeast Asia. For the first time, we reveal the relationship of neutral winds and the MTM to the postmidnight FAIs. In addition, we study the mechanisms responsible for generating postmidnight FAIs at low latitudes.

2. Observations

The observation sites in Southeast Asia that were used in this study are shown in Figure 1. The EAR is located at Kototabang, Indonesia (0.2°S, 100.3°E; dip latitude 10.4°S) and was used to observe 3 m scale FAIs. An ionosonde, an all-sky airglow imager, and a Fabry-Perot interferometer (FPI) are collocated at this site (red star in figure). More than 120 GPS receivers (magenta points in figure) were in operation at the time in Indonesia and Malaysia. Two other ionosondes, one each installed at Chumphon (10.7°N, 99.4°E, dip latitude 3.3°N) and Chiang Mai (18.8°N, 98.9°E, dip latitude 13.0°N) in Thailand were used in this study. The EAR, which was installed in 2001, has a peak power of 100 kW and a beam width of 3.4° [*Fukao et al.*, 2003a]. Because the operating frequency of the EAR is 47.0 MHz, 3 m scale FAIs in the ionosphere can be detected as coherent echoes of the radar beam perpendicular to the magnetic field lines. The EAR can steer the radar beams
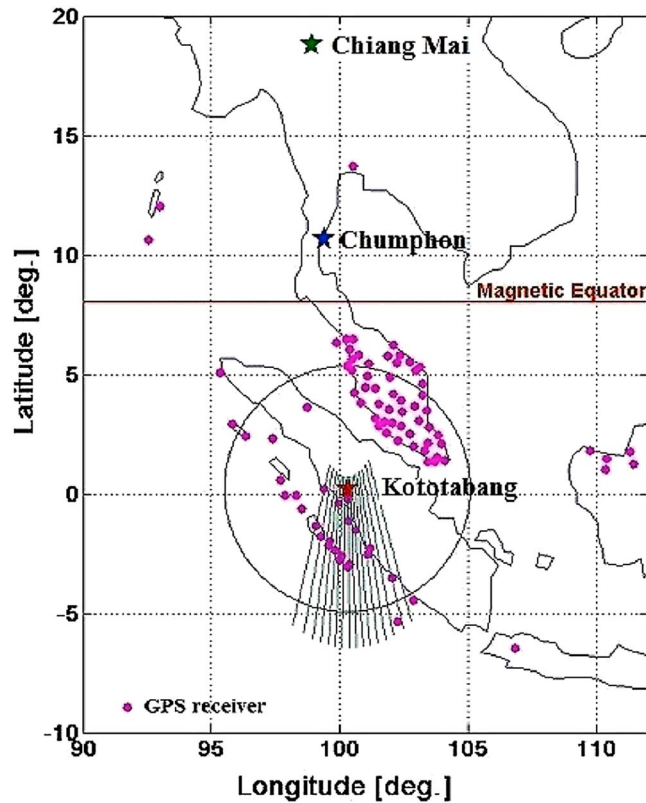
Figure 1. Map of the observation sites. The red star represents the location of Kototabang, where the EAR, an airglow imager, an FPI, and an ionosonde are hosted. The circle represents the field of view (FOV) of the airglow imager; its radius is 500 km (which corresponds to approximately 70° off zenith when the airglow layer is assumed to exist at an altitude of 250 km). The fan-shaped lines represent the EAR radar beams that are projected along the magnetic field to an altitude of 250 km. The magenta dots represent the locations of GPS receivers. The blue and green stars represent the locations of ionosondes at Chumphon and Chiang Mai, respectively.

rapidly on a pulse-by-pulse basis by means of an active phased-array antenna system. Multibeam observations can be used to perceive the spatial structure of 3 m scale FAIs in the *F* region of the ionosphere [*Fukao et al.*, 2003b, 2004; *Yokoyama and Fukao*, 2006; *Dao et al.*, 2016]. Nighttime ionospheric FAI measurements have been carried out routinely since May 2010. As described by *Yokoyama et al.* [2011], one cycle of observations takes approximately 140 s and consists of four measurement modes: (1) three sets of single-beam *F* region FAI measurement, (2) two sets of eight-beam *F* region FAI measurement, (3) two sets of three-beam *E* region FAI measurements, and (4) lower atmosphere observations. The three sets of single-beam *F* region FAI measurements provide a radar echo spectrum with a Doppler spectral width of ±398 m/s. For the eight-beam *F* region FAI measurements, by scanning the radar beam on a pulse-to-pulse basis, FAI echoes are measured simultaneously in the eight beam directions practically. Combining the two sets of eight-beam measurements, a two-dimensional map of the echo intensity in a fan-shaped range-azimuth sector is obtained every 140 s. The
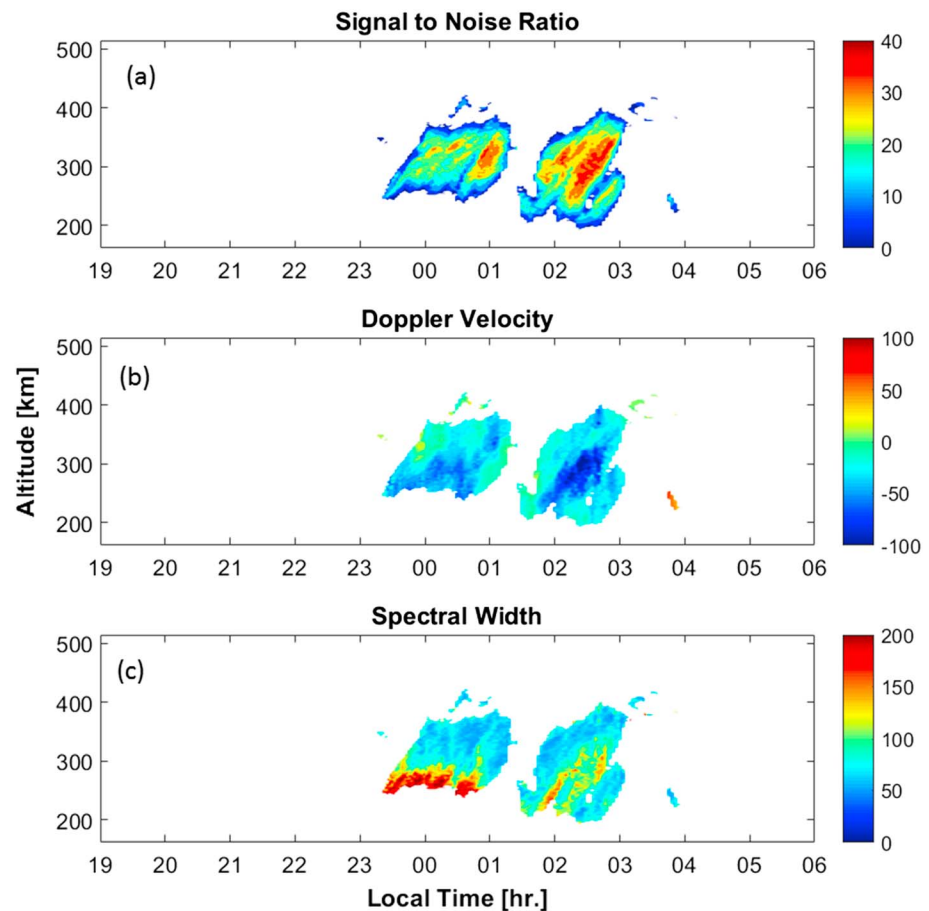
locations of the FAI measurements on the 16 beams are projected along the magnetic field (solid lines in Figure 1) onto a surface at an altitude of 250 km.

The GPS receiver networks in Southeast Asia are useful for studying the extension and development of equatorial plasma bubbles in the region. In our study, the total electron content (TEC) was calculated from the GPS data obtained from the networks of IGS, SuGAr, and MyRTKnet (the last is operated by the Department of Survey and Mapping (JUPEM), Malaysia [*Buhari et al.*, 2014]) via the Scripps Orbit and Permanent Array Center (SOPAC) website and the National Institute of Information and Communications Technology (NICT) database. The rate of TEC change index (ROTI) is defined as the standard deviation of the rate of TEC change over 5 min. The ROTI was calculated for each satellite-receiver pair and mapped on an ionospheric shell at an altitude of 300 km with a latitude-longitude pixel size of 0.15° × 0.15°. The ROTI can indicate the occurrence of irregularities on a scale of a few kilometers [*Otsuka et al.*, 2006; *Nishioka et al.*, 2008]. Therefore, using the two-dimensional ROTI maps, the horizontal structures of the plasma bubbles that contain kilometer-scale irregularities can be investigated.

An all-sky airglow imager has been in operation at Kototabang since 2002 as part of the optical mesosphere thermosphere imagers (OMTIs) [*Shiokawa et al.*, 2009]. All-sky images of the 630 nm airglow intensity are obtained every 5.5 min with an exposure time of 165 s. An oxygen line with a wavelength of 630.0 nm is emitted from the lower thermosphere at altitudes of 200–300 km. Its intensity is proportional to the product of the plasma and atomic oxygen densities. Therefore, the two-dimensional structures of plasma bubbles can be detected in the 630 nm airglow images as airglow intensity depletions. In Figure 1, the FOV of the airglow

Figure 2. Altitude-time cross sections of (a) signal-to-noise ratio (SNR), (b) Doppler velocity (positive toward the radar), and (c) spectral width observed on a beam of 180° azimuth with the EAR at Kototabang, Indonesia on the night of 9 July 2010.

images is represented by a circle with a radius of 500 km, corresponding to approximately 70° off zenith when the airglow layer is assumed to exist at an altitude of 250 km. The airglow imager's FOV covers the location of the EAR radar beam projected onto the 250 km altitude, hence the airglow structure can be compared with the FAI echo region. A low-cost compact FPI has been in operation at Kototabang since 2010 as part of the OMTIs [*Shiokawa et al.*, 2012]. It consists of a 70 mm etalon and a highly sensitive cooled charge-coupled device (CCD) camera using 1024 × 1024 pixels to obtain the interference fringes of the weak airglow emission. A sky scanner is located above the FPI optics to point in any direction. During routine FPI observations, this direction is changed sequentially (north, south, east, then west) with a zenith angle of 45° and a 3.5 min exposure time for each direction. The FPI etalon produces 10 interference fringes per image. The line-of-sight velocity and neutral temperature are measured from the Doppler velocity and broadening associated with the differences in location and width of each fringe, respectively. In this study, we take the average value obtained from the 10 fringes in an image. Four line-of-sight velocities are combined to obtain the horizontal meridional and zonal components of the neutral wind. We assume that the neutral wind velocity is uniform within the FPI FOV and that the vertical component of the neutral wind is negligible relative to the horizontal component. The temperature estimated from FPI was also presented thoroughly by *Nakamura et al.* [2017].

Three ionosondes have been installed along the 100°E magnetic meridian at Kototabang, Chiang Mai, and Chumphon in the past decade. These ionosondes belong to the Southeast Asia Low-latitude Ionospheric Network (SEALION) [*Maruyama et al.*, 2007]. Kototabang and Chiang Mai form a pair of nearly magnetically conjugate points, connecting the Northern and Southern Hemispheres by magnetic field lines; Chumphon is located near the magnetic equator. The height variation between those two locations is useful for deriving the thermospheric winds in the magnetic meridional plane [*Maruyama et al.*, 2008; *Saito et al.*, 2008]. In this
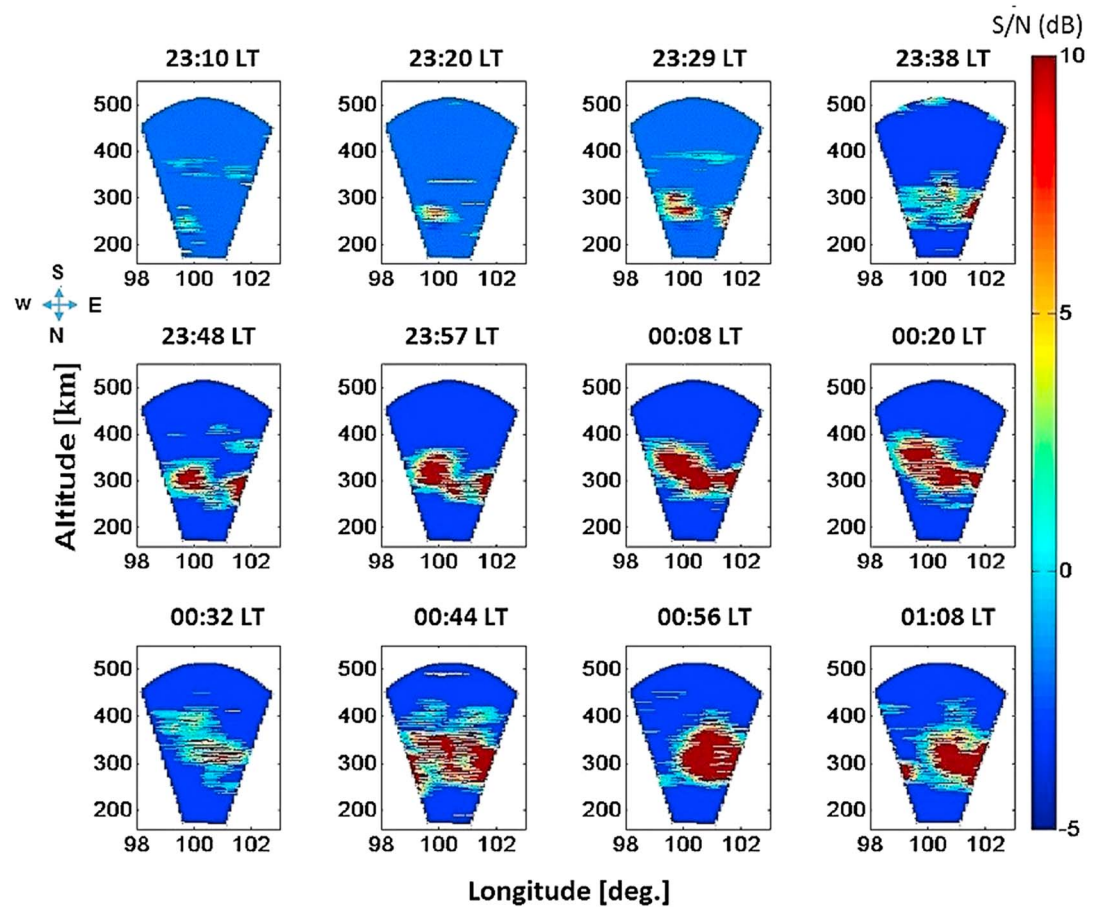
Figure 3. Time sequence of fan-shaped range-azimuth sector plots of SNR observed with the EAR from 2310 LT on 9 July 2010 to 0108 LT on the next day.

study, the virtual height of the F layer, $h'F$, is used to measure variations in the altitude of the bottomside of the F layer.

3. Results

In this section, we present observational results of the effects of thermospheric neutral wind on the occurrence of a FAI on the night of 9 July 2010. First, the postmidnight FAI detected by the EAR is shown in Figure 2. Figure 2a shows range-time intensity plots of the signal-to-noise ratio (SNR) observed on a beam with a 180° azimuth and a 23.8° zenith, on which FAIs first appeared at an altitude of 250 km at around 2320 LT and subsequently extended to higher altitudes. The other FAI echoes were detected at 0130 LT. This echo region extended to higher altitudes with time and persisted until 0300 LT. Figures 2b and 2c show the Doppler velocity (positive toward the radar) and spectral width, respectively, as functions of local time and altitude over the same period as in Figure 2a. The Doppler velocity of the FAI echo is upward and southward (negative values). Large spectral widths (up to 200 m/s) were observed at the underside of the FAI echo regions between 2320 and 0100 LT. These features indicate that the FAI in this event was in the generation phase.

We use a pair of eight-beam EAR measurements to view the spatial structure of the FAI echoes in a plane perpendicular to the magnetic field to investigate the spatial and temporal variations of the FAIs. Figure 3 shows a time sequence of two-dimensional maps of the SNR observed with the EAR on the night of 9 July 2010. In this figure, a FAI echo was observed at an altitude of 250 km within the FOV of the EAR at around 2310 LT, and subsequently developed to higher altitudes. Another FAI echo was also detected at the eastern side of the EAR's FOV at 2329 LT. The first echo region extended to higher altitudes, moved slowly eastward and
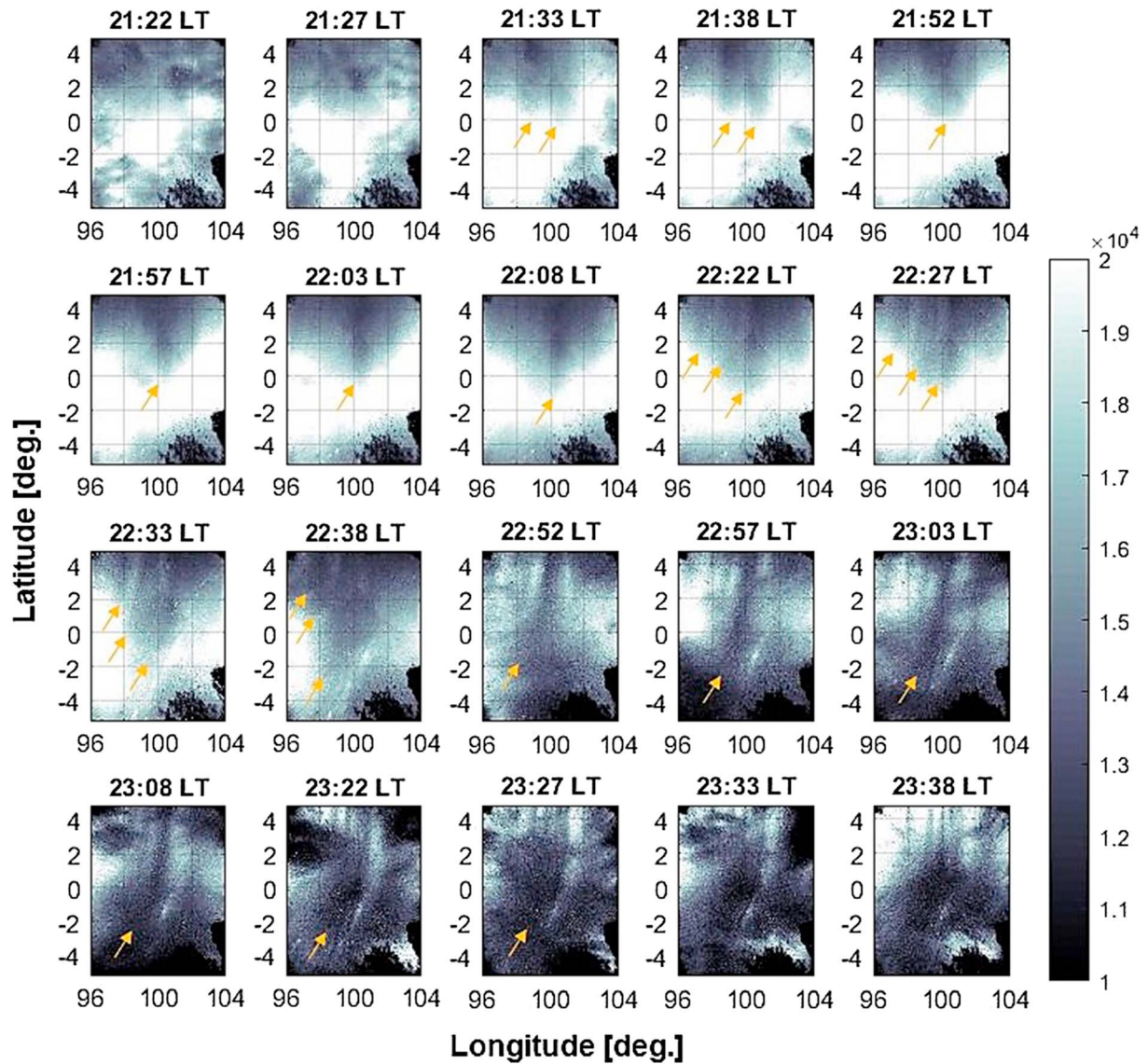
Figure 4. Time sequence of airglow images observed with the all-sky airglow imager at Kototabang, Indonesia from 2122 to 2338 LT on 9 July 2010. The yellow arrows indicate the plasma bubble.

merged with the other echo region at 0008 LT. The FAI echo region kept moving eastward after 0032 LT while changing shape. Another FAI echo region appeared at the western side of the FOV at 0108 LT. This echo region corresponds to the FAI that appeared between 0130 and 0300 LT, as shown in Figure 2.

A time sequence of 630 nm airglow images taken with the all-sky imager at Kototabang on the night of 9 July 2010 is shown in Figure 4. In these images, airglow depletions extending along the north-south direction are seen as darker colors. These low-intensity structures correspond to plasma bubbles. In the figure, plasma bubbles can be seen in the FOV of the airglow imager from 2133 LT (denoted by the yellow arrows). Note that the structures of the plasma bubbles could not be seen before 2127 LT because of clouds. Two band-like plasma bubble structures appeared between 2133 and 2138 LT, but the western airglow depletion dimmed from 2152 LT and kept the same shape until 2208 LT. From 2222 until 2238 LT, two other small plasma bubbles existed. Between 2227 and 2238 LT, one of the plasma bubbles extended southward and reached 3–4°S. From 2252 LT, only one plasma bubble existed, lasting for more than 30 min. It was difficult to detect plasma bubbles after 2333 LT because of clouds. A feature to which we pay attention in this study is that the plasma bubble extended southward rapidly at around 2230 LT.
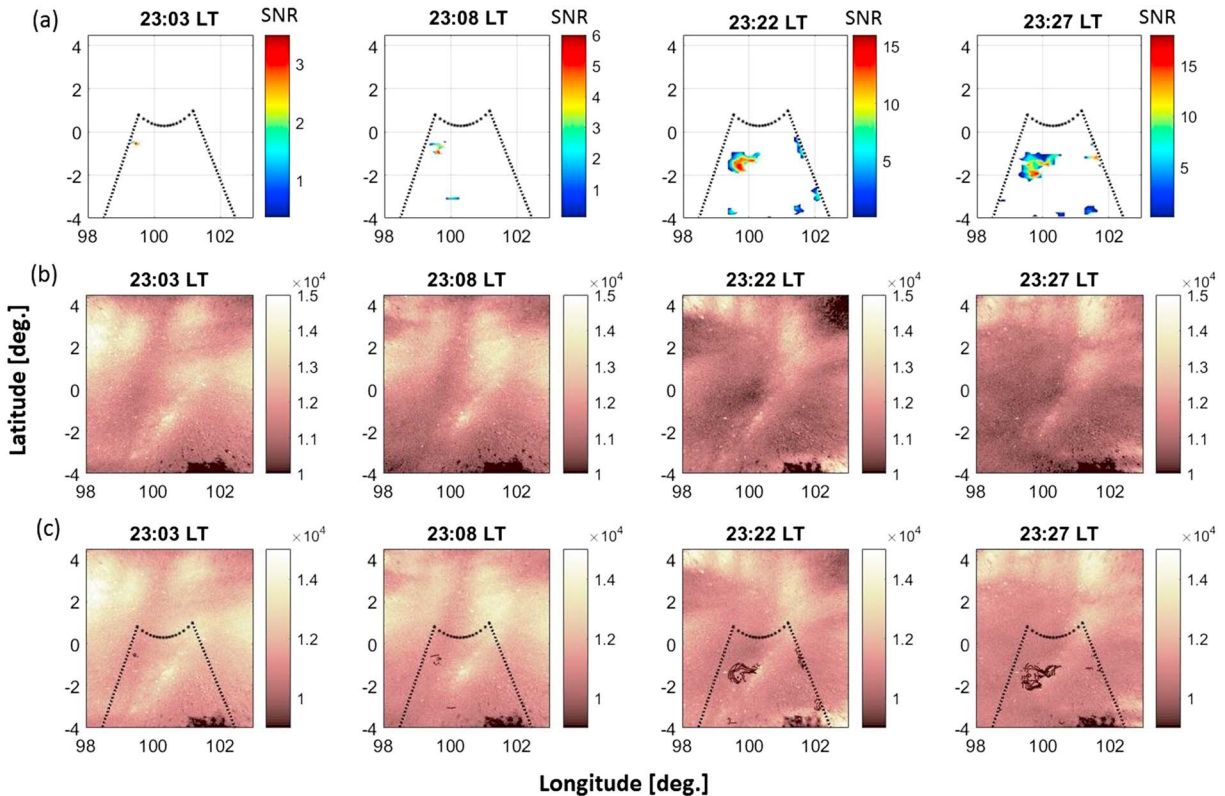
Figure 5. (a) Distribution of FAI echo intensity (SNR) observed with the EAR from 2303 to 2327 LT on 9 July 2010. The SNR is mapped along the magnetic field lines onto a horizontal plane at an altitude of 250 km. (b) The 630 nm airglow images taken by the all-sky airglow imager at the EAR site. (c) Airglow images of Figure 5b overlain with the FAI echo intensities shown in Figure 5a. The contour lines are drawn above the 0 dB level at 3 dB intervals. The fan-shaped black lines represent the EAR's FOV on this 250 km plane.

To investigate the locations of the FAIs and plasma bubbles, we projected the observed FAI echo intensity along the magnetic field onto a horizontal plane at an altitude of 250 km. Figures 5a and 5b show distributions of the FAI echo intensity (SNR) observed with the EAR and 630 nm airglow images taken by the all-sky airglow imager at the EAR site from 2303 to 2327 LT on 9 July 2010. In Figure 5c, the instantaneous FAI echo intensity is superposed on each airglow image. Contour lines are drawn above the 0 dB level at 3 dB intervals. The fan-shaped black lines represent the EAR's FOV on this 250 km plane. As shown in Figure 5c, a faint FAI echo was first observed at 2303 in the western side of the EAR's FOV at 0.2°S within the plasma depletion. Thus, we observed postmidnight FAIs that clearly existed inside a plasma bubble and were generated after 2300 LT.

We now use GPS data from Southeast Asia to investigate the ROTI, which represents the existence of kilometer-scale plasma density irregularities. Figure 6 shows a time sequence of ROTI maps charted on the ionospheric shell at an altitude of 300 km between 2020 and 0020 LT on 9 July 2010. The ROTI enhancement elongating in the north-south direction appeared at the western edge of the FOV of the ROTI map between 2°N and 4°N at 2040 LT and then moved eastward. The ROTI values increased with time between 2020 and 2110 LT, and decreased after 2130 LT. The plasma density irregularities represented by the ROTI existed in a plasma bubble that was generated at the western side of the FOV and moved eastward. The decrease in ROTI values after 2130 LT was due to the earlier disappearance of smaller-scale irregularities due to diffusion across the magnetic field. The ROTI values then increased between 2250 and 2310 LT, and this enhanced region extended to higher latitudes. By comparing with the airglow images in Figure 4, we can see the coexistence of a plasma bubble and few-kilometer-scale irregularities represented by the ROTI. However, the ROTI values increased 20 min after the plasma bubble extended to higher latitudes.

We examine the temporal variation of ROTI enhancement at longitudes around Kototabang. Figure 7a shows latitude and local time variations of ROTI values on the night of 9 July 2010. The maximum ROTI values over
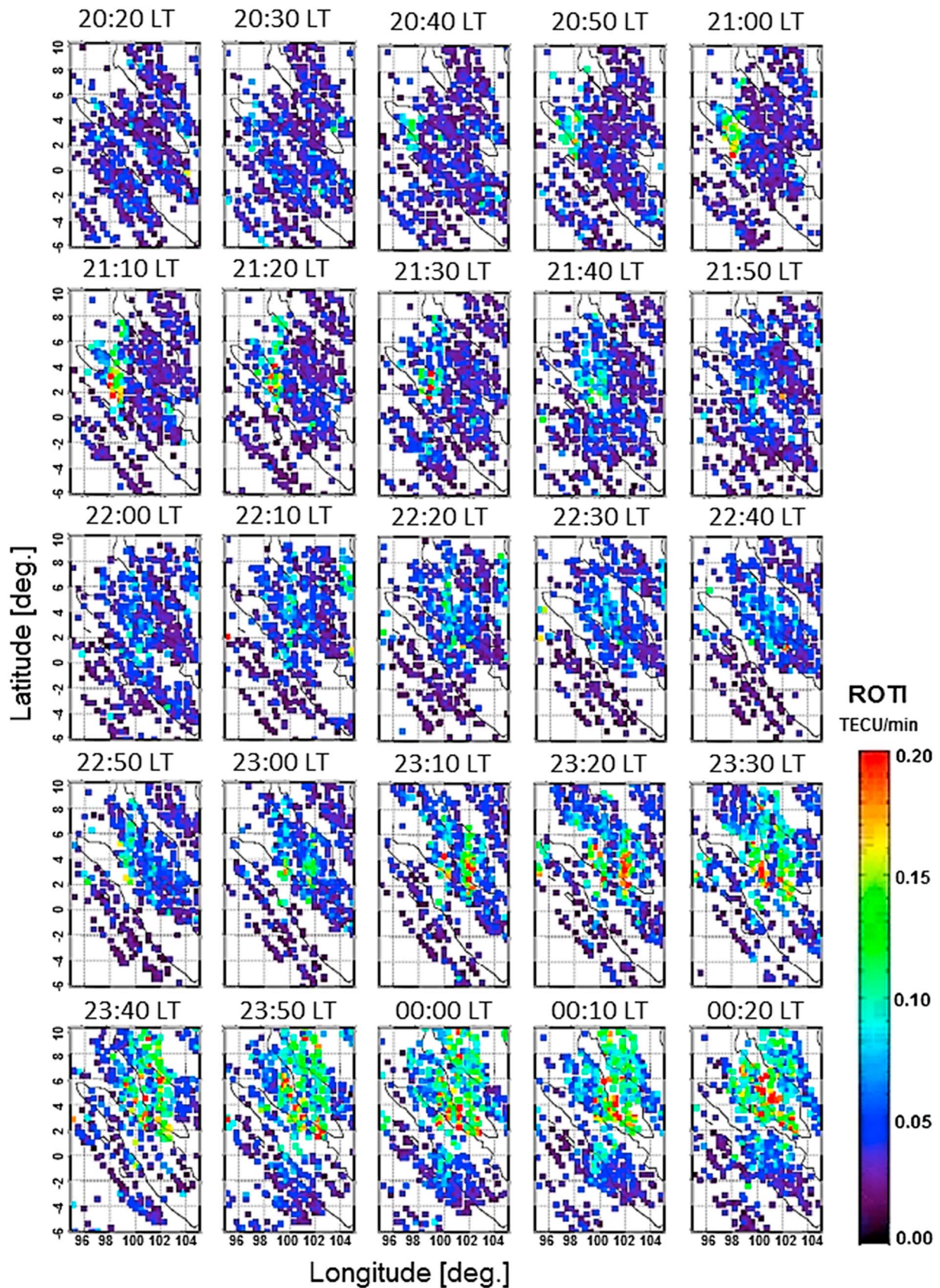
Figure 6. Time sequence of maps showing ROTI in Southeast Asia from 2020 LT on 9 July 2010 to 0020 LT on the next day.
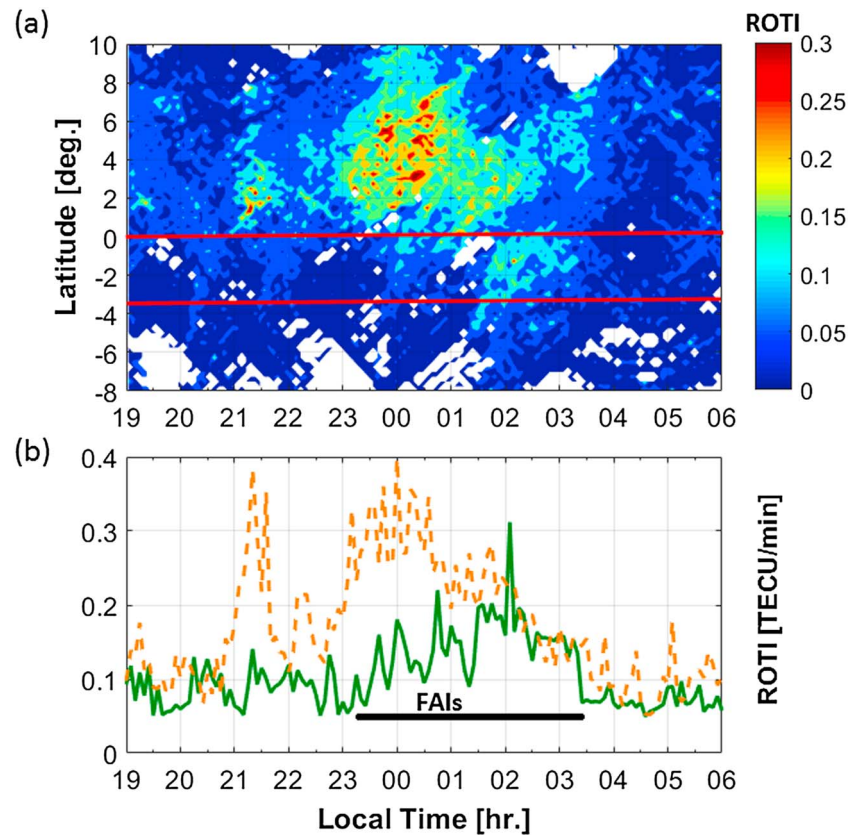
Figure 7. (a) Latitude and local time variations of ROTI observed by GPS receivers in Southeast Asia on the night of 9 July 2010. The two horizontal red lines denote the EAR's FOV in the *F* region (250 and 400 km altitudes) mapped onto a horizontal plane at an altitude of 250 km. (b) Local time variation of maximum ROTI in the latitudes of the EAR's FOV (green line) and those of 2–5°N (orange line). The black line represents the time period during which FAIs were observed with the EAR.

98–103°E are selected at every latitude grid. This shows that the first ROTI enhancement occurred between 2050 and 2150 LT. Another one appeared at 2250 LT, extending rapidly northward and southward after 2300 LT and reaching the latitude of Kototabang (0.2°S) around midnight. The two red horizontal lines in the figure represent the latitudes at which the magnetic field lines connecting to the EAR's southward beam at altitudes of 250 and 400 km cross a horizontal plane at an altitude of 300 km. The green line in Figure 7b shows the temporal variation of the maximum ROTI value within the latitudes of the EAR FOV (0–3.6°S). The orange dashed line represents the temporal variation of the maximum ROTI value over 2–5°N, wherein the ROTI enhancement was strongest. We can see that the ROTI near the magnetic equator increased dramatically at 2300 LT. By comparing with the airglow images shown in Figure 4, the ROTI enhancement is found to appear 30 min after the plasma bubble extended to higher latitudes. Based on the green line, ROTI enhancement exceeding 0.15 TECU/min within the EAR's FOV can be seen between 2330 and 0315 LT. The black line in the figure represents FAI echoes that lasted from 2310 to 0330 LT. The ROTI enhancement is found to coincide with the FAIs observed by the EAR, although the ROTI enhancement started 20 min after the FAI appearance.

In order to reveal the mechanisms whereby the plasma bubble extended to higher latitudes between 2230 and 2300 LT, we examine the *F* layer altitude (*h'F*) observed with the three ionosondes and compare this with the thermospheric neutral winds and temperatures observed by the FPI at Kototabang. Coordinated observations of these parameters are presented in Figure 8. Figure 8a shows local time variations of *h'F* at Chiang Mai, Chumphon, and Kototabang. The *h'F* values at Kototabang (Chiang Mai) increased by approximately 100 km from 2230 (2245) to 0015 (0000) LT, whereas those at Chumphon did not show a significant change. This indicates a weak zonal electric field and that the rise of the *F* layer at low latitudes could have been caused by equatorward neutral winds. As shown in Figure 8b, there was
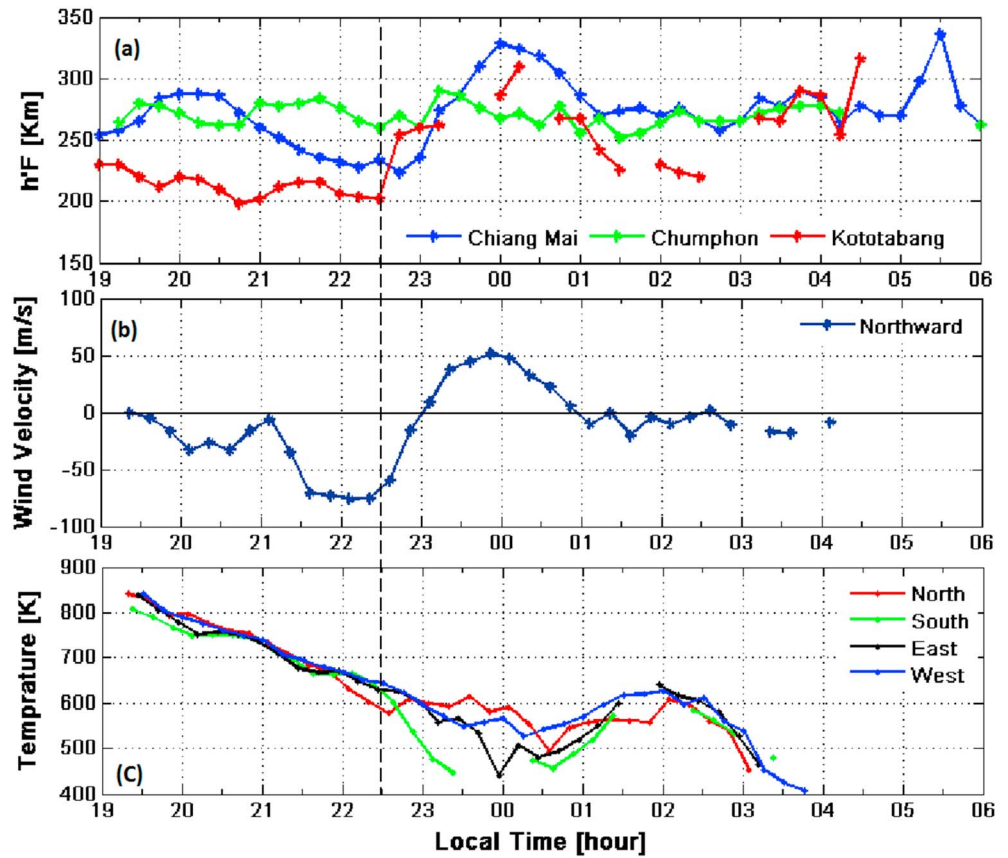
Figure 8. (a) Local time variations of virtual height of the *F* layer (*h'F*) at Chiang Mai, Chumphon, and Kototabang. (b) Thermospheric neutral winds and (c) thermospheric temperature on the night of 9 July 2010. The virtual height was measured with ionosondes. The thermospheric neutral wind and temperature were measured with the FPI at Kototabang, Indonesia. The vertical dashed line indicates 2230 LT, when the virtual height at Kototabang started to increase.

a persistent southward (magnetically poleward) wind of around 75 m/s from 2130 to 2225 LT. The southward wind started to decrease at 2230 LT, which is almost the same time at which the *h'F* values at Kototabang and Chiang Mai started to increase. This decrease of the southward wind can be considered as an enhancement of the northward wind. The meridional neutral wind changed its direction to northward at 2300 LT and northward wind reached a peak of approximately 50 m/s at midnight. Note that because the magnetic latitude of Kototabang is 10°S (a magnetic inclination of −17°), a northward wind corresponds to a geomagnetically equatorward wind, which pushes the ionosphere up to higher altitudes along the magnetic field lines. Figure 8c shows temporal variation of the thermospheric neutral temperature observed in four directions at Kototabang. Neutral temperatures were estimated from each fringe. We eliminated the temperature below 400 K since such underestimation of the temperature occurs due to contamination of OH emission from mesopause region when the 630 nm airglow intensity is weak [*Nakamura et al.*, 2017]. We then obtained the neutral temperature with a standard deviation less than 60 K as estimated from the 10 fringes. As shown in this figure, the neutral temperatures observed in the four directions decreased with time after sunset. From 2300 to 0000 LT, the neutral temperature in the north remained almost constant at around 600 K, whereas the temperatures in the other directions continued to decrease. As a result, the temperature is higher at the north of Kototabang between 2300 and 0020 LT. This result suggests that MTM is likely located at the north of Kototabang, where is in the Northern Hemisphere. After 0030 LT, the neutral temperature in all directions increased and reached a peak at around 0200 LT. These results suggest that the high-temperature region moved from north to south through the location of Kototabang.

4. Discussion

Around midnight on 9 July 2010, FAIs were observed with the EAR. Based on the local-time, season, and solar-activity behavior of FAIs, these ones can be classed as postmidnight FAIs [*Nishioka et al.*, 2012; *Ajith et al.*, 2015; *Dao et al.*, 2016]. During this event, airglow depletions caused by plasma bubbles were observed by the all-sky airglow imager at Kototabang. The postmidnight FAIs of this event were shown to be generated within the plasma bubbles. From a time sequence of airglow images, we also found that the plasma bubbles grew southward (higher magnetic latitudes) around 2230 LT. This plasma bubble growth coincided with the uplift of the *F* layer at both Kototabang and Chiang Mai. In contrast, the altitude of the *F* layer at Chumphon, which is located near the magnetic equator, did not show any significant variation during this event. These results suggest that magnetically equatorward winds at low latitudes in both the Northern and Southern Hemispheres could uplift the *F* layer to higher altitudes. Direct observation of the neutral winds at Kototabang using an FPI showed weakening of the poleward wind followed by an equatorward wind coinciding with the ascent of the *F* layer. Poleward winds push the *F* region plasma downward along the magnetic field lines to lower altitudes, so a weakening of the poleward wind could result in the *F* layer rising.

The linear growth rate γ of the RT instability, which is responsible for generating plasma bubbles, is given by [*Zalesak and Ossakow*, 1982; *Sultan*, 1996]

$$\gamma = \frac{\sum_P^F}{\sum_P^E + \sum_P^F}\left(\frac{E}{B} - u_n - \frac{g}{v_{in}}\right)\frac{1}{N}\frac{\partial N}{\partial z} - R$$

where *E* is the eastward electric field, *B* is the magnetic field, u_n is the flux-tube-integrated neutral wind perpendicular to the magnetic field in the magnetic meridian plane (positive upward/poleward) weighted by the Pedersen conductivity, *g* is the acceleration due to gravity (taken to be negative), v_{in} is the flux-tube-integrated ion-neutral collision frequency weighted by the plasma density, and *N* is the flux-tube-integrated electron content in the *F* region. The terms $\sum_P^F$ and $\sum_P^E$ are the flux-tube-integrated *F* and *E* region Pedersen conductivities, respectively, and *R* is the chemical recombination rate. The growth rate γ is proportional to $\left(\frac{E}{B} - u_n - \frac{g}{v_{in}}\right)$, which drives an eastward Pedersen current because polarization electric fields are generated to keep the current continuity.

Using a physics-based model, *Yizengaw et al.* [2013] suggested that the eastward electric field formed by the appearance of sporadic-*E* cloud at night over the June solstice could lead to the formation of postmidnight plasma bubbles via RT instabilities. On the night of 9 July 2010, however, the *F* layer altitude at Chumphon, which is located near the magnetic equator, did not show any significant variation. Consequently, the zonal electric field *E* in this event could have been weak, making it negligible in relation to the RT growth rate. At Chiang Mai, which is close to the magnetically conjugate point of Kototabang, the *F* layer ascent was observed with an ionosonde at almost the same time as the *F* layer ascent at Kototabang. When the *F* layer ascends to higher altitudes, at which the neutral density is low, γ increases because the ion-neutral collision frequency v_{in} decreases with altitude. The simultaneous ascents of the *F* layer in both the Northern and Southern Hemispheres during the present event enhanced the growth rate γ.

The equatorward neutral wind contributes to increase of the growth rate in two ways. The parallel component of the neutral winds along the magnetic field at low latitudes drags ions along the field lines up to higher altitudes where v_{in} is smaller. The equatorward perpendicular component (u_n) combined with *B* drives an eastward Pedersen current. Consequently, γ could increase where the magnetic field pierces the low-latitude ionosphere, where Kototabang and Chiang Mai are located. This could explain why the plasma bubble grew at magnetically low latitudes around midnight when the equatorward component of the neutral wind was enhanced. *Huba and Krall* [2013] used the NRL ionospheric model SAMI3/ESF to study the impact of meridional winds on the growth of RT instabilities. They found that the equatorward winds destabilize the bottomside of the *F* region for the RT instability, which is consistent with the observations presented in this paper. According to their interpretation, the parallel component of the neutral wind along the geomagnetic field carries the plasma to higher altitudes, thereby reducing the Pedersen conductivity so that the bottomside of the *F* layer is destabilized by RT instabilities. They also pointed out that the eastward Pedersen current induced by the equatorward wind helps to increase the RT growth rate. Their simulated equatorward-wind convergence from both hemispheres can produce destabilizing effects leading to plasma bubbles. Our observational results of neutral winds in this paper are consistent with their simulation.
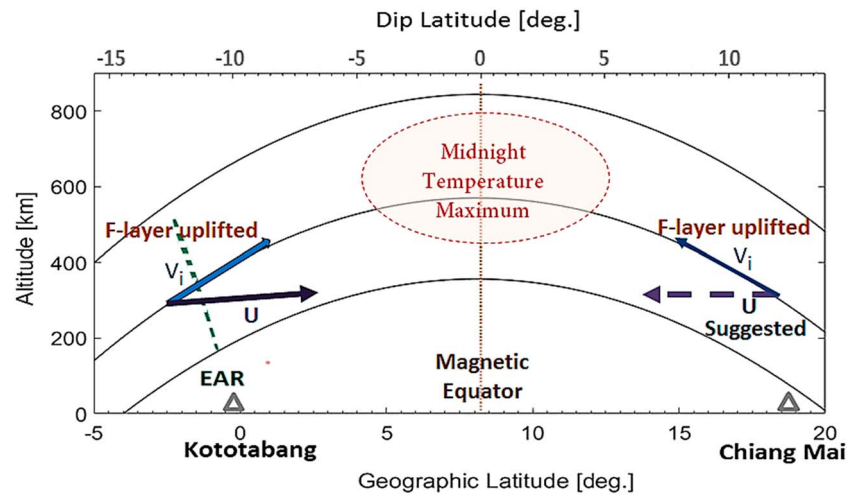
Figure 9. Schematic showing relationship between meridional thermospheric winds and *F* layer uplift at magnetically low latitudes. *F* layer uplift was observed at Kototabang and Chiang Mai. Equatorward wind enhancement was observed at Kototabang. The MTM could have been located between Kototabang and Chiang Mai.

In this event, although plasma depletion was observed with the all-sky airglow imager within the FOV of the EAR, FAIs were not observed until 2303 LT. They appeared just after the meridional wind over Kototabang became equatorward at 2300 LT. Simultaneously, irregularities on the scale of a few kilometers, represented by ROTI, also occurred. These results suggest that equatorward winds contribute to the generation and/or intensification of plasma density irregularities. The equatorward winds at magnetically low latitudes drive an eastward Pedersen current via the ion motion in the $u \times B$ direction, and gravity always generates an eastward Pedersen current because of $g \times B$ ion drift. Therefore, as mentioned above, the equatorward wind at magnetically low latitudes could intensify the eastward current, which in turn could generate large polarization electric fields in the plasma bubbles to maintain the continuity of the electric current. These large polarization electric fields could play an important role in plasma instabilities, resulting in plasma density irregularities. Lower hybrid drift instabilities or low-frequency drift waves could generate meter-scale irregularities [*Huba et al.*, 1978; *Huba and Ossakow*, 1979]. In the present event, the appearance of the few-kilometer-scale irregularities detected by the GPS receivers coincided with the occurrence of FAIs corresponding to 3 m scale irregularities when the meridional neutral wind turned equatorward. These results suggest that equatorward winds contributed to the generation of those irregularities.

Figure 9 shows the relationship between equatorward wind and *F* layer ascent at Kototabang and Chiang Mai, which are located at low latitudes. Because the zonal electric field was relatively weak in this event, the *F* layer ascent over Chiang Mai could also have been caused by equatorward winds. Therefore, we can consider that the winds were equatorward in both Northern and Southern Hemispheres, indicating convergence of the thermospheric winds. *Fesen* [1996] reported that convergence of the meridional winds at low latitudes causes compressional heating, resulting in a local maximum in the neutral temperature, namely the MTM. When such wind convergence occurred, the thermospheric neutral temperature to the north of Kototabang was higher than that in the other directions. These results suggest that an MTM could have existed and that there could have been a peak in the neutral temperature at the north of Kototabang. The neutral temperature increased in all directions with a peak around 0200 LT indicates that the high temperature region propagated from north to south through the location of Kototabang. The transported location of this neutral temperature is consistent with movements of midnight density maximum structure simulated by the Whole Atmosphere model [*Akmaev et al.*, 2010] as well as the extensions of MTM observed by AEE satellite at solstice [*Herrero and Spencer*, 1982].

Our results suggest that uplift of the *F* layer, which could play an important role in generating postmidnight FAIs, could be caused by magnetically equatorward thermospheric winds associated with an MTM. The tendency for FAIs to occur at midnight could be related to the dependence of the MTM on the local time. Regarding the seasonal variation of MTMs, *Fesen* [1996] and *Herrero and Spencer* [1982] have reported that

MTMs occur most frequently in summer. *Fesen* [1996] also presented that the development of the MTM is due to the upward propagating semidiurnal tides. The 2, 2 and 2, 3 tidal modes may reinforce each other in summer causing the maximum occurrence of MTM in this time period. Around the June solstice, a peak in thermospheric temperature due to an MTM could occur between 10°N and 20°N. The winds converging toward the center of the thermospheric temperature peak would become magnetically equatorward winds at both Kototabang and Chiang Mai. Around the December solstice, the peak in thermospheric temperature due to the MTM is located in the Southern Hemisphere between 10°S and 20°S [*Herrero and Spencer*, 1982; *Akmaev et al.*, 2010] and therefore could be at magnetic latitudes higher than Kototabang. In that case, the converging winds that contributed to the MTM formation would be poleward at Kototabang. Although this would correspond to an equatorward wind at Chiang Mai, Chiang Mai is far from the thermospheric temperature peak and thus the wind could be relatively weak. Consequently, we suggest that seasonal variation in the location of the thermospheric temperature related to the MTM corresponds to the seasonal variation of the occurrence of postmidnight FAIs. Furthermore, *Niranjan et al.* [2006] have suggested that the rate of MTM occurrence is higher in conditions of low solar activity. This is also consistent with the solar-activity dependence of the postmidnight FAIs, suggesting that MTM occurrence may contribute to the generation of postmidnight FAIs.

5. Conclusions

We presented observational results from a postmidnight FAI event observed with the EAR on the night of 9 July 2010. We compared these with all-sky 630 nm airglow images, kilometer-scale plasma irregularities, *F* layer altitudes, and thermospheric neutral winds and temperatures. Our findings in relation to this particular event are summarized as follows. (1) The postmidnight FAIs were collocated with a plasma bubble and coincided with kilometer-scale irregularities. (2) The plasma bubble grew to higher latitude when the *F* layer at Kototabang and Chiang Mai rose and the equatorward thermospheric wind was enhanced at Kototabang. (3) A northward gradient of thermospheric temperature was observed at Kototabang at the same time as the enhancement of northward winds and during the occurrence of postmidnight FAIs.

We suggest that the convergence of equatorward neutral winds from the Northern and Southern hemispheres could be associated with a MTM occurring around the magnetic equator. Equatorward neutral winds can uplift the *F* layer at low latitudes and increase the growth rate of Rayleigh-Taylor instability, causing more rapid extension of plasma bubbles. The equatorward thermospheric winds in both hemispheres could also intensify the eastward current that generates the large polarization electric field. The intensified current could then generate a large polarization electric field within the plasma bubble to maintain the continuity of the electric current. The large polarization electric fields could also cause plasma instabilities, resulting in plasma density irregularities. Therefore, postmidnight FAIs are generated within plasma bubbles. This case study provides observational evidence for the role of the equatorward thermospheric winds at low latitudes in the growth of plasma bubbles at midnight and the generation of postmidnight FAIs.

References

Ajith, K. K., S. T. Ram, M. Yamamoto, T. Yokoyama, V. S. Gowtam, Y. Otsuka, T. Tsugawa, and K. Niranjan (2015), Explicit characteristics of evolutionary-type plasma bubbles observed from equatorial atmosphere radar during the low to moderate solar activity years 2010–2012, *J. Geophys. Res. Space Physics*, *120*, 1371–1382, doi:10.1002/2014JA020878.

Akmaev, R. A., F. Wu, T. J. Fuller-Rowell, H. Wang, and M. D. Iredell (2010), Midnight density and temperature maxima, and thermospheric dynamics in Whole Atmosphere Model simulations, *J. Geophys. Res.*, *115*, A08326, doi:10.1029/2010JA015651.

Basu, S., S. Basu, J. Aarons, J. P. McClure, and M. D. Cousins (1978), On the coexistence of kilometer- and meter-scale irregularities in the nighttime equatorial F region, *J. Geophys. Res.*, *83*, 4219–4226, doi:10.1029/JA083iA09p04219.

Buhari, S. M., M. Abdullah, A. M. Hasbi, Y. Otsuka, T. Yokoyama, M. Nishioka, and T. Tsugawa (2014), Continuous generation and two-dimensional structure of equatorial plasma bubbles observed by high-density GPS receivers in Southeast Asia, *J. Geophys. Res. Space Physics*, *119*, 10,569–10,580, doi:10.1002/2014JA020433.

Burke, W. J., L. C. Gentile, C. Y. Huang, C. E. Valladares, and S. Y. Su (2004), Longitudinal variability of equatorial plasma bubbles observed by DMSP and ROCSAT-1, *J. Geophys. Res.*, *109*, A12301, doi:10.1029/2004JA010583.

Candido, C. M. N., I. S. Batista, F. Becker-Guedes, M. A. Abdu, J. H. A. Sobral, and H. Takahashi (2011), Spread F occurrence over a southern anomaly crest location in Brazil during June solstice of solar minimum activity, *J. Geophys. Res.*, *116*, A06316, doi:10.1029/2010JA016374.

Dao, E., M. C. Kelley, P. Roddy, J. Retterer, J. O. Ballenthin, O. de La Beaujardiere, and Y.-J. Su (2011), Longitudinal and seasonal dependence of nighttime equatorial plasma density irregularities during solar minimum detected on the C/NOFS satellite, *Geophys. Res. Lett.*, *38*, L10104, doi:10.1029/2011GL047046.

Dao, T., Y. Otsuka, K. Shiokawa, S. Tulasi Ram, and M. Yamamoto (2016), Altitude development of postmidnight F region field-aligned irregularities observed using equatorial atmosphere radar in Indonesia, *Geophys. Res. Lett.*, *43*, 1015–1022, doi:10.1002/2015GL067432.

Fejer, B. G., E. R. de Paula, S. A. Gonzalez, and R. F. Woodman (1991), Average vertical and zonal F region plasma drifts over Jicamarca, *J. Geophys. Res.*, *96*, 13,901–13,906, doi:10.1029/91JA01171.

Fesen, C. G. (1996), Simulations of the low-latitude midnight temperature maximum, *J. Geophys. Res.*, *101*, 26,863–26,874, doi:10.1029/96JA01823.

Fukao, S., H. Hashiguchi, M. Yamamoto, T. Tsuda, T. Nakamura, M. K. Yamamoto, T. Sato, M. Hagio, and Y. Yabugaki (2003a), Equatorial Atmosphere Radar (EAR): System description and first results, *Radio Sci.*, *38*(3), 1053, doi:10.1029/2002RS002767.

Fukao, S., Y. Ozawa, M. Yamamoto, and R. T. Tsunoda (2003b), Altitude-extended equatorial spread F observed near sunrise terminator over Indonesia, *Geophys. Res. Lett.*, *30*(22), 2137, doi:10.1029/2003GL018383.

Fukao, S., Y. Ozawa, T. Yokoyama, M. Yamamoto, and R. T. Tsunoda (2004), First observations of the spatial structure of F region 3-m-scale field-aligned irregularities with the equatorial atmosphere radar in Indonesia, *J. Geophys. Res.*, *109*, A02304, doi:10.1029/2003JA010096.

Herrero, F. A., and N. W. Spencer (1982), On the horizontal distribution of the equatorial thermospheric midnight temperature maximum and its seasonal variation, *Geophys. Res. Lett.*, *9*, 1179–1182, doi:10.1029/GL009i010p01179.

Herrero, F. A., N. W. Spencer, and H. G. Mayr (1993), Thermosphere and F-region plasma dynamics in the equatorial region, *Adv. Space Res.*, *13*, 201–220.

Huba, J. D., and J. Krall (2013), Impact of meridional winds on equatorial spread F: Revisited, *Geophys. Res. Lett.*, *40*, 1268–1272, doi:10.1002/grl.50292.

Huba, J. D., and S. L. Ossakow (1979), On the generation of 3-m irregularities during equatorial spread F by low-frequency drift waves, *J. Geophys. Res.*, *84*, 6697–6700, doi:10.1029/JA084iA11p06697.

Huba, J. D., P. K. Chaturvedi, S. L. Ossakow, and D. M. Towle (1978), High frequency drift waves with wavelengths below the ion gyroradius in equatorial spread F, *Geophys. Res. Lett.*, *5*, 695–698, doi:10.1029/GL005i008p00695.

Li, G., B. Ning, M. A. Abdu, X. Yue, L. Liu, W. Wan, and L. Hu (2011), On the occurrence of postmidnight equatorial F region irregularities during the June solstice, *J. Geophys. Res.*, *116*, A04318, doi:10.1029/2010JA016056.

Maruyama, T., M. Kawamura, S. Saito, K. Nozaki, H. Kato, N. Hemmakorn, T. Boonchuk, T. Komolmis, and C. Ha Duyen (2007), Low latitude ionosphere-thermosphere dynamics studies with ionosonde chain in Southeast Asia, *Ann. Geophys.*, *25*, 1569–1577.

Maruyama, T., S. Saito, M. Kawamura, and K. Nozaki (2008), Thermospheric meridional winds as deduced from ionosonde chain at low and equatorial latitudes and their connection with midnight temperature maximum, *J. Geophys. Res.*, *113*, A09316, doi:10.1029/2008JA013031.

Meriwether J., M. Faivre, C. Fesen, P. Sherwood, and O. Veliz (2008), New results on equatorial thermospheric winds and the midnight temperature maximum, *Ann. Geophys.*, *26*, 447–466.

Nakamura, Y., et al. (2017), Measurement of thermospheric temperatures using OMTI Fabry–Perot interferometers with 70-mm etalon, *Earth Planets Space*, doi:10.1186/s40623-017-0643-1.

Niranjan, K., P. S. Brahmanandam, and B. Srivani (2006), Signatures of equatorial midnight temperature maximum as observed from in situ and ground-based ionospheric measurements in the Indian sector, *J. Geophys. Res.*, *111*, A07309, doi:10.1029/2005JA011386.

Nicolls, M. J., M. C. Kelley, M. N. Vlasov, Y. Sahai, J. L. Chau, D. L. Hysell, P. R. Fagundes, F. Becker-Guedes, and W. L. C. Lima (2006), Observations and modeling of post-midnight uplifts near the magnetic equator, *Ann. Geophys.*, *24*, 1317–1331.

Nishioka, M., A. Saito, and T. Tsugawa (2008), Occurrence characteristics of plasma bubble derived from global ground-based GPS receiver networks, *J. Geophys. Res.*, *113*, A05301, doi:10.1029/2007JA012605.

Nishioka, M., Y. Otsuka, K. Shiokawa, T. Tsugawa, Effendy, P. Supnithi, T. Nagatsuma, and K. T. Murata (2012), On post-midnight field-aligned irregularities observed with a 30.8-MHz radar at a low latitude: Comparison with F-layer altitude near the geomagnetic equator, *J. Geophys. Res.*, *117*, A08337, doi:10.1029/2012JA017692.

Otsuka, Y., K. Shiokawa, T. Ogawa, T. Yokoyama, M. Yamamoto, and S. Fukao (2004), Spatial relationship of equatorial plasma bubbles and field-aligned irregularities observed with an all-sky airglow imager and the equatorial atmosphere radar, *Geophys. Res. Lett.*, *31*, L20802, doi:10.1029/2004GL020869.

Otsuka, Y., et al. (2006), GPS detection of total electron content variations over Indonesia and Thailand following the 26 December 2004 earthquake, *Earth Planets Space*, *58*, 159–165, doi:10.1186/BF03353373.

Otsuka, Y., T. Ogawa, and Effendy (2009), VHF radar observations of nighttime F-region field-aligned irregularities over Kototabang, Indonesia, *Earth Planets Space*, *61*, 431–437.

Otsuka, Y., K. Shiokawa, M. Nishioka, and Effedy (2012), VHF radar observations of post-midnight F-region field-aligned irregularities over Indonesia during solar minimum, *Indian J. Radio Space Phys.*, *41*, 199–207.

Patra, A. K., D. V. Phanikumar, and T. K. Pant (2009), Gadanki radar observations of F region field-aligned irregularities during June solstice of solar minimum: First results and preliminary analysis, *J. Geophys. Res.*, *114*, A12305, doi:10.1029/2009JA014437.

Saito, S., S. Fukao, M. Yamamoto, Y. Otsuka, and T. Maruyama (2008), Decay of 3-m-scale ionospheric irregularities associated with a plasma bubble observed with the equatorial atmosphere radar, *J. Geophys. Res.*, *113*, A11318, doi:10.1029/2008JA013118.

Shiokawa, K., Y. Otsuka, and T. Ogawa (2009), Propagation characteristics of nighttime mesospheric and thermospheric waves observed by optical mesosphere thermosphere imagers at middle and low latitudes, *Earth Planets Space*, *61*, 479–491.

Shiokawa, K., Y. Otsuka, S. Oyama, S. Nozawa, M. Satoh, Y. Katoh, Y. Hamaguchi, Y. Yamamoto, and J. Meriwether (2012), Development of low-cost sky-scanning Fabry-Perot interferometers for airglow and auroral studies, *Earth Planets Space*, *64*, 1033–1046.

Sultan, P. J. (1996), Linear theory and modeling of the Rayleigh-Taylor instability leading to the occurrence of equatorial spread F, *J. Geophys. Res.*, *101*, 26,875–26,891, doi:10.1029/96JA00682.

Tsunoda, R. T. (1985), Control of the seasonal and longitudinal occurrence of equatorial scintillations by the longitudinal gradient in integrated E-region Pedersen conductivity, *J. Geophys. Res.*, *90*, 447–456, doi:10.1029/JA090iA01p00447.

Tsunoda, R. T., R. C. Livingston, J. P. McClure, and W. B. Hanson (1982), Equatorial plasma bubbles: vertically elongated wedges from the bottomside F layer, *J. Geophys. Res.*, *87*(A11), 9171–9180, doi:10.1029/JA080i011p09171.

Woodman, R. F., and C. Lahoz (1976), Radar observations of F region equatorial irregularities, *J. Geophys. Res.*, *81*, 5447–5466, doi:10.1029/JA081i031p05447.

Yizengaw, E., J. Retterer, E. E. Pacheco, P. Roddy, K. Groves, R. Caton, and P. Baki (2013), Postmidnight bubbles and scintillations in the quiet-time June solstice, *Geophys. Res. Lett.*, *40*, 5592–5597, doi:10.1002/2013GL058307.

Yokoyama, T., and S. Fukao (2006), Upwelling backscatter plumes in growth phase of equatorial spread F observed with the equatorial atmosphere radar, *Geophys. Res. Lett.*, *33*, L08104, doi:10.1029/2006GL025680.

Yokoyama, T., M. Yamamoto, Y. Otsuka, M. Nishioka, T. Tsugawa, S. Watanabe, and R. F. Pfaff (2011), On postmidnight low-latitude ionospheric irregularities during solar minimum: 1. Equatorial atmosphere radar and GPS-TEC observations in Indonesia, *J. Geophys. Res.*, *116*, A11325, doi:10.1029/2011JA016797.

Zalesak, S. T., and S. L. Ossakow (1982), On the prospect for artificially inducing equatorial spread *F*, Memo. Rep. 4899, Nay. Res. Lab., Washington, D. C.